Internal waves in a shear background current: Transition from solitary-wave regime to dispersive-wave regime

Chengzhu Xu [*]

Department of Civil Engineering, University of Calgary, Calgary, Alberta, Canada T2N 1N4

Marek Stastna

Department of Applied Mathematics, University of Waterloo, Waterloo, Ontario, Canada N2L 3G1

Nonlinear internal waves propagating in a quasi-two-layer stratification with a shear background current are investigated by means of high-resolution direct numerical simulations. The simulations are performed in a two-dimensional rectangular domain, representing a laboratory-scale tank of finite length. The internal waves are generated using the lock-release mechanism, while the background shear currents are induced by basin-scale internal seiches created using a tilted tank suddenly returned to the untilted configuration. Both mechanisms are readily realizable in a laboratory environment. Depending on the configuration of the initial density profile, both internal solitary-like waves (ISWs) and finite-amplitude dispersive wave trains (DWTs) may be observed in the simulations. The ISWs are observed when the pycnocline is located relatively far away from the middepth and/or the background shear is oriented against the wave-induced velocity shear. Comparison of the waveforms observed in the simulations to those described by the fully nonlinear Dubreil-Jacotin–Long (DJL) theory suggests that these waves are indeed solitary-like, implying that laboratory experiments of ISWs propagating in a shear background current can be realized in a relatively straightforward manner. As the pycnocline approaches the middepth and/or the background shear reverses its polarity and increases its magnitude, the waves tend to have a smaller amplitude and a larger half-width. When a wave's amplitude is less than approximately 3% of its half-width, the dispersive effect becomes dominant and the wave loses its solitary-like form. In this case, a finite-amplitude DWT is formed instead, in which the leading wave has a reduced propagation speed from the ISW propagation speed. Analysis based on the DJL theory suggests that exact solitary waves of similar amplitude in such a background environment have an extremely large half-width that is on the same order of magnitude as the finite length of the simulation domain, implying that their formation cannot be supported in a laboratory environment.

I. INTRODUCTION

Over the past decades, field observations have demonstrated that large-amplitude, high-frequency, nonlinear internal waves are ubiquitous features of coastal oceans. These waves are mainly generated from stratified flows (particularly tidal flows) over rough topographical features on the ocean floor, such as ridges, seamounts, and canyons [1]. One of the most commonly observed types of nonlinear internal waves is internal solitary and solitary-like waves (ISWs) [2,3] whose waveforms are maintained by a balance between nonlinear steepening and dispersive spreading.

---

[*]chengzhu.xu@ucalgary.ca

In open waters with a relatively constant background environment (e.g., stratification and current), these waves may propagate over a long distance without substantially changing form. Nevertheless, there are circumstances in which such a balance is lost and the waves are no longer solitary-like. This could happen, for example, during the fissioning process, in which an ISW of depression shoals upon a gentle slope and reverses its polarity when the pycnocline center passes the middepth, thereby producing a dispersive wave train (DWT) [4,5].

In addition to sloping topography that leads to wave shoaling, the presence of a shear background current can also significantly alter the waveforms and even the nature of the limit on wave amplitude of ISWs [6]. In particular, stratifications that may preclude wave breaking without a shear current may lead to wave breaking when a background shear current is present. This can have implications for enhanced mixing, material transport, and possibly even sediment resuspension. For example, Lamb and Farmer [7] observed an ISW on the Oregon shelf and showed that, in the presence of a background current with near-surface shear, an ISW of depression could develop a trapped surface core, leading to the onset of convective instabilities. This result implies that the interaction of the wave with a near-surface background current can profoundly change the occurrence of instabilities in the wave. For sediment resuspension, Bogucki *et al.* [8] analyzed ISWs of elevation propagating on the California shelf in the presence of a near-bottom background current oriented against the direction of wave propagation. The passage of the ISWs was accompanied by an increased concentration of particulate matter in the water column. Their observation has motivated many subsequent studies of boundary-layer instabilities and sediment resuspension induced by ISW–boundary-layer interaction, as discussed in a recent review [9].

While ISWs propagating in a shear background current have been observed in the field and documented in the literature, investigations using laboratory experiments are lacking. This is primarily because in a laboratory tank, the finite length of the tank imposes a significant constraint on how a shear current can be created. One commonly used method for generating shear flow is to fill an initially tilted tank with stratified fluid and then release the tank so that the tilted density interface starts to evolve [10,11], creating an internal standing wave (i.e., internal seiche). However, the resulting shear flow is not spatially or temporally uniform and hence may not be well approximated by the type of idealized parallel flow that is convenient for theoretical studies. Moreover, as degeneration of the initial seiche takes place, seiches may break down into solitary waves, bores, and/or billows [11,12].

Traveling internal waves (e.g., ISWs) are typically generated using the lock-release mechanism in a laboratory tank [13–15]. The tank is initially filled with a stably stratified fluid of two or more layers, with a gate place near one end of the tank. Behind the gate, a volume of light fluid (or heavy fluid, depending on the experimental setup) is added to create a depression (or elevation, if heavy fluid is used) in the density field. Once the gate is released, the initial depression (or elevation) develops into a train of traveling waves which propagates along the pycnocline toward the other end of the tank. The initial condition needs to be set up carefully in order to yield waves of desired form. Mathematical theory for the initial-value problem for weakly nonlinear equations such as the Korteweg–de Vries (KdV) equation and Gardner equation (the latter is referred to as the eKdV in [3]) exists; see, for example, Sec. 2.3 of [16]. However, the authors are not aware of any instance in the literature where this theory was applied to an internal wave experiment, and in practice laboratory initial conditions are adjusted on a trial and error basis [17].

The present work aims to identify a viable method for studying the problem of internal wave dynamics in a shear background current in a laboratory environment, by investigating the interaction of ISWs and DWTs with basin-scale internal seiches. The results presented here are obtained from high-resolution direct numerical simulations performed in a two-dimensional rectangular domain, which represents a laboratory-scale tank of finite length. The traveling waves are generated using the lock-release mechanism, while the seiches are created using a tilted tank suddenly returned to the untilted configuration, both of which are readily realizable in laboratory experiments. The waves obtained from the simulations are compared to those described by the fully nonlinear theory, in order to identify the regime in which ISWs can exist and the regime in which only dispersive waves can form.

The remainder of this paper is organized as follows. The theoretical description of ISWs in a vertically varying background current is presented in Sec. II. The problem is formulated in Sec. III. The simulation results are presented in Secs. IV and V, with Sec. IV focusing on ISWs and Sec. V focusing on DWTs and the connection to Gardner equation theory. The findings of this work are summarized and discussed in Sec. VI.

II. THEORETICAL BACKGROUND

A. Fully nonlinear theory

Fully nonlinear ISWs can be computed by solving the Dubreil-Jacotin–Long (DJL) equation, an eigenvalue problem for the isopycnal displacement $\eta(x, z)$ and the solitary-wave propagation speed c in a channel of finite depth H. The isopycnal displacement measures the vertical displacement of the isopycnal relative to its undisturbed state in the far-upstream location. In the presence of a background current $U(z)$ and under the Boussinesq approximation, the DJL equation takes the form [6]

$$\nabla^2\eta + \frac{U_z(z - \eta)}{U(z - \eta) - c}\big[1 - \eta_x^2 - (1 - \eta_z)^2\big] + \frac{N^2(z - \eta)}{[U(z - \eta) - c]^2}\eta = 0, \tag{1}$$

with the boundary conditions $\eta(x, 0) = \eta(x, H) = 0$ and $\eta(x, z) \to 0$ as $x \to \pm\infty$. In this equation, subscripts denote ordinary and partial derivatives, and N^2 is the square of the buoyancy frequency defined by

$$N^2(z) = -g\frac{d\bar{\rho}}{dz}, \tag{2}$$

where g is the gravitational acceleration and $\bar{\rho}(z)$ is the undisturbed *dimensionless* density profile (i.e., the density profile scaled by the reference density ρ_0) in the far field.

The DJL equation is equivalent to the full set of stratified Euler equations in the steady state, i.e., in a reference frame moving with the wave. In the derivation of the DJL equation, no assumption with respect to the nonlinearity of the fluid flow is made. Hence, solutions of the DJL equation are exact solitary-wave solutions in the inviscid limit. For large-amplitude waves, these solutions have been shown to be different from waveforms predicted by weakly nonlinear theories, such as the KdV equation and its higher-order extensions [18,19]. This conclusion also holds for borelike solutions [20], referred to as DWTs in the present work.

For nonconstant N, the DJL equation does not have analytical solutions. In the present work, the DJL equation is solved numerically using the method described in [21]. The algorithm is based on the variational scheme developed in [22], which seeks a solution iteratively that minimizes the kinetic energy, subject to the constraint that the available potential energy (APE) is held fixed. The APE is a functional that maps the field η to the scalar A and when scaled by $\rho_0 gH$ in a two-dimensional domain is given by [19]

$$A(\eta) = \frac{1}{H}\int_0^H \int_{-\infty}^{\infty} \int_0^{\eta} [\bar{\rho}(z - \eta) - \bar{\rho}(z - s)]ds\,dx\,dz. \tag{3}$$

The APE measures the amount of potential energy that can be converted into kinetic energy and is specified *a priori* when solving for the DJL equation, while other wave parameters are determined implicitly by the algorithm.

By solving for the DJL equation in prespecified background currents, Stastna and Lamb [6] showed that the presence of a shear background current not only affects an ISW's propagation speed and half-width, but also alters the nature of the upper bound on wave amplitude. In particular, for a linear background current, the maximum amplitude an ISW can have depends on the sign and the strength of the background vorticity. In a background current whose vorticity has the same sign as the ISW-induced current, increasing the strength of the background vorticity decreases the maximum amplitude an ISW can have. In certain extreme cases, the polarity of the ISW may also

be reversed. On the other hand, if the background vorticity has the opposite sign to the ISW-induced current, then ISWs of extremely large amplitude can exist, though such waves may develop a region of low Richardson numbers and hence become unstable.

B. Weakly nonlinear theory

Weakly nonlinear theories can provide qualitative guidance in a semianalytical setting. For a two-layer fluid (which is a good approximation of the stratification profiles used herein), the Gardner equation (following the notation of [3]) is given as

$$\eta_t + (c_0 + \alpha_1 \eta + \alpha_2 \eta^2)\eta_x + \beta_1 \eta_{xxx} = 0, \tag{4}$$

where $\eta(x, t)$ represents the displacement of the interface from its far upstream rest height, and the various parameters are given as closed-form expressions in terms of the layer thicknesses. The Gardner equation has solitary-wave solutions that subsume the classical sech^2 soliton solution of the KdV equation. When the interface lies near the middepth, the Gardner equation predicts flat crested waves, in agreement with the exact DJL theory. The fidelity of the Gardner equation's predictions of the maximum possible wave amplitude decays as the interface moves from the middepth (see, for example, Fig. 9 of [23]). Nevertheless, the Gardner equation can provide a ready guide to the parameter space and will be used for this below. When a background shear current is present, the various parameters in (4) no longer have a closed form and solving the DJL equation for exact waves is numerically as convenient as the approximate theory.

III. PROBLEM FORMULATION

Numerical simulations presented in this work are performed in a two-dimensional rectangular domain with a length $L = 16$ m and a depth $H = 0.4$ m, though different lengths have also been considered. With a shorter domain, breaking down of the seiche into solitary waves and/or the onset of shear instability is likely to happen [11,12], while longer domains are beyond the limit of a reasonable laboratory setting. A right-handed Cartesian coordinate system is adopted, with the origin fixed at the lower left corner of the domain, the x axis directed to the right along the flat bottom, and the z axis pointing up toward the surface. Free-slip boundary conditions are used in both horizontal and vertical directions.

The governing equations for the present work are the incompressible Navier-Stokes equations under the Boussinesq and rigid lid approximations [24], given by

$$\frac{D\mathbf{u}}{Dt} = -\nabla p - \rho g \hat{k} + \nu \nabla^2 \mathbf{u}, \tag{5a}$$

$$\nabla \cdot \mathbf{u} = 0, \tag{5b}$$

$$\frac{D\rho}{Dt} = \kappa \nabla^2 \rho, \tag{5c}$$

where $\mathbf{u} = (u, w)$ is the velocity field, ρ is the density field, p is the pressure field, g is the acceleration due to gravity, ν is the kinematic viscosity, and κ is the molecular diffusivity. As is the common practice under the Boussinesq approximation, the equations are in dimensional form, except that the density ρ and the pressure p are scaled by the reference density ρ_0. The effect of the earth's rotation is neglected.

All simulations were carried out using the numerical model described and validated in [25]. The model employs a spectral collocation method [26], which yields highly accurate results. As appropriate for the boundary conditions, the Fourier sine or cosine transform is used, depending on the variable of interest. For an optimal combination of the accuracy and computational efficiency, the grid size is chosen to be $N_x \times N_z = 8192 \times 512$, which gives a horizontal grid spacing of approximately 1.95 mm and a vertical grid spacing of approximately 0.78 mm. In all simulations, the viscosity and diffusivity are fixed at $\nu = 1 \times 10^{-6}$ m^2/s and $\kappa = 2 \times 10^{-7}$ m^2/s, which together
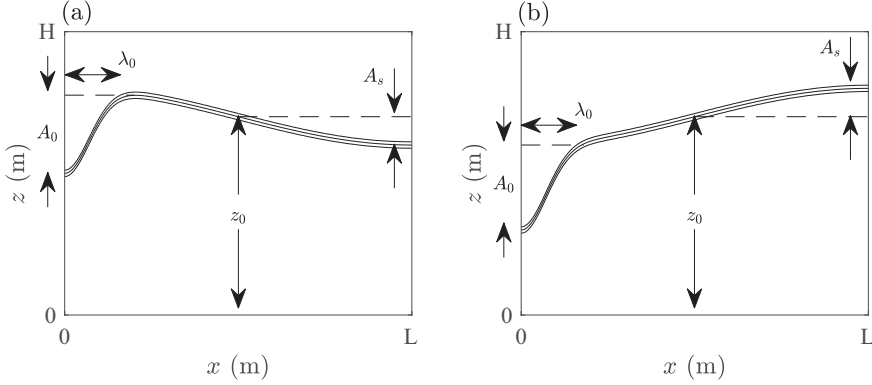
FIG. 1. Schematic diagrams of the initial density field, with the initial wave generated at the seiche's (a) crest and (b) trough.

give a Schmidt (or Prandtl) number $Sc = \nu/\kappa = 5$. This value is chosen because recent work by Xu *et al.* [27] has shown that the diffusive effect plays an important role in the "viscous" adjustment of ISWs and that the value $Sc = 1$, as often adopted by literature reporting "direct numerical simulations" [28,29], is not necessarily the best choice.

In order to obtain shear currents that are nearly parallel, we consider basin-scale internal seiches with a single node, whose wavelength is set by L. The initial density field, illustrated in Fig. 1, consists of a quasi-two-layer stratification with a dimensionless density difference $\Delta\rho = 0.01$ and a pycnocline whose half-width is $d = 0.01$ m. The analytical form of the initial density profile, nondimensionalized by the reference density ρ_0, is given by

$$\rho(x, z) = 1 - 0.5\Delta\rho \tanh\left\{\frac{z - z_0 - A_s \cos(\pi x/L) + A_0 \exp[-(x/\lambda_0)^2]}{d}\right\}. \tag{6}$$

In this equation, z_0 represents the height of the node of the seiche (i.e., the average height of the pycnocline in the absence of an ISW), A_s is the amplitude of the seiche, A_0 is the amplitude of the depression in the initial density field, and λ_0 is the length of the initial depression. The pycnocline is centered above the middepth, so in the absence of a shear current ISWs are waves of depression. The region of light fluid is always located near the left boundary of the domain, so waves generated from this region propagate to the right initially. This region can be located at either the crest or the trough of the seiche, depending on the sign of A_s. In particular, Fig. 1(a) illustrates the scenario of positive A_s, while Fig. 1(b) illustrates the scenario of negative A_s. The initial velocity field is identically zero.

In a two-layer stratification with a zero background current, the linear long-wave speed is defined by

$$c_{lw} = \sqrt{\Delta\rho g \frac{z_0(H - z_0)}{H}}. \tag{7}$$

It sets the upper bound for the phase and group speeds of small-amplitude periodic waves but the lower bound for the propagation speed of finite-amplitude solitary-like waves. In a quasi-two-layer stratification with the presence of a background current, it can still provide a good estimate for the characteristic velocity scale of internal wave propagation, provided the pycnocline is thin relative to the layer thickness and the background current is weak relative to the wave-induced current. Based on the two-layer long-wave speed and the half-depth of the domain, the Reynolds-number estimate for the present model setup is given by

$$\text{Re} = \frac{c_{lw}H}{2\nu}. \tag{8}$$

TABLE I. List of simulations presented in Sec. IV, with parameters for the initial density profile given in Eq. (6). The dimensionless parameters, labeled with a tilde, are scaled by H. In the case labels, C (T) indicates that the initial wave is generated at the crest (trough) of the seiche and I indicates that there is no seiche in the background. The number indicates the depression in the initial density field (i.e., A_0 measured in 10^{-2} m).

Case	Dimensional parameters				Dimensionless parameters			
	z_0 (m)	A_s (m)	A_0 (m)	λ_0 (m)	$\tilde{z}_0$	$\tilde{A}_s$	$\tilde{A}_0$	$\tilde{\lambda}_0$
Cases in which the ISW is generated at the seiche's crest								
C10	0.32	0.02	0.1	0.5	0.8	0.05	0.25	1.25
C15	0.32	0.02	0.15	0.5	0.8	0.05	0.375	1.25
C20	0.32	0.02	0.2	0.5	0.8	0.05	0.5	1.25
C25	0.32	0.02	0.25	0.5	0.8	0.05	0.625	1.25
Cases with ISW only (i.e., no seiche)								
I10	0.32	0	0.1	0.5	0.8	0	0.25	1.25
I15	0.32	0	0.15	0.5	0.8	0	0.375	1.25
I20	0.32	0	0.2	0.5	0.8	0	0.5	1.25
I25	0.32	0	0.25	0.5	0.8	0	0.625	1.25
Cases in which the ISW is generated at the seiche's trough								
T10	0.32	−0.02	0.1	0.5	0.8	−0.05	0.25	1.25
T15	0.32	−0.02	0.15	0.5	0.8	−0.05	0.375	1.25
T20	0.32	−0.02	0.2	0.5	0.8	−0.05	0.5	1.25
T25	0.32	−0.02	0.25	0.5	0.8	−0.05	0.625	1.25
Cases with seiche only (i.e., no ISW)								
C0	0.32	0.02	0	0.5	0.8	0.05	0	1.25
T0	0.32	−0.02	0	0.5	0.8	−0.05	0	1.25

We note that this choice of Reynolds number, while convenient, does not account for wave amplitude and thus would not be appropriate for wave-induced instabilities, or other effects with a strong amplitude dependence. Finally, note that in the Gardner equation (4), as given in [3], the linear long-wave speed is labeled as c_0.

IV. SOLITARY-WAVE REGIME

A. Parameter space

Numerical simulations presented in this section are listed in Table I, together with their dimensional and dimensionless parameters. Here we focus on the dynamics of internal solitary-like waves by setting $z_0 = 0.32$ m, which is equivalent to 80% of the total depth. In this stratification, the two-layer long-wave speed is $c_{lw} \approx 0.08$ m/s and the estimated Reynolds number is Re $\approx 1.6 \times 10^5$. As we will show later in this section, the traveling waves we studied are indeed solitary-like and hence will be referred to as the ISWs or simply the waves, while the standing waves in the background will be referred to as the seiches in order to distinguish from the traveling waves. We consider background currents induced by seiches with amplitudes $A_s = \pm 0.02$ m. Since the ISWs are generated near the left boundary and propagate to the right, the wave-induced vorticity is always positive. Hence, the seiche-induced vorticity has the opposite sign to the wave-induced vorticity if $A_s > 0$ but the same sign if $A_s < 0$. For comparison, ISWs propagating in a zero background current are also considered (by setting $A_s = 0$). The parameter A_0 is varied between 0.1 and 0.25 m in order to obtain waves of different amplitudes, while the parameter λ_0 is tuned to be 0.5 m in order for the initial conditions to yield single-crest solitary waves in the absence of a background current. Additionally, simulations with seiches only (by setting $A_0 = 0$) are also performed in order to provide the background states for quantitative measurement.
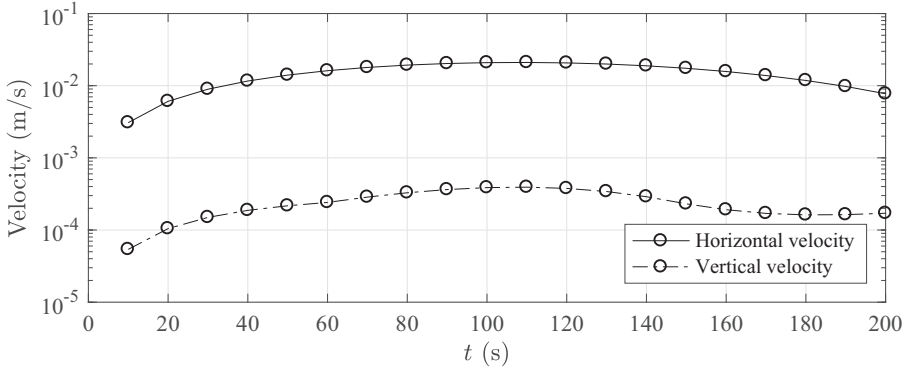
FIG. 2. Time series plot of the maximum seiche-induced horizontal velocity (solid curve) and vertical velocity (dash-dotted curve) for the case C0 from $t = 10$ to 200 s.

We let $\mathbf{U} = (U, W)$ denote the background velocity induced by the seiche. For simulations presented in this section, $\mathbf{U}$ can be approximated by the velocity fields of C0 or T0, because the background shear current does not change its features during the propagation of ISWs. For the case C0, Fig. 2 shows the maximum seiche-induced horizontal and vertical velocities (in terms of absolute value) from $t = 10$ to 200 s. The figure suggests that the vertical velocity is always two orders of magnitude smaller than the horizontal velocity and hence does not have a significant influence on the flow dynamics. The figure also shows that, at least near $t = 100$ s, the change of horizontal velocity with respect to time is relatively small and is not difficult for the solitary waves to adjust to. At $t = 100$ s, we also computed the local gradient Richardson number using the formula

$$\mathrm{Ri} = \frac{N^2}{U_z^2} \tag{9}$$

and found that the minimum Richardson number is 7.06, implying that it is not possible for the onset of shear instability in the present flow regime.
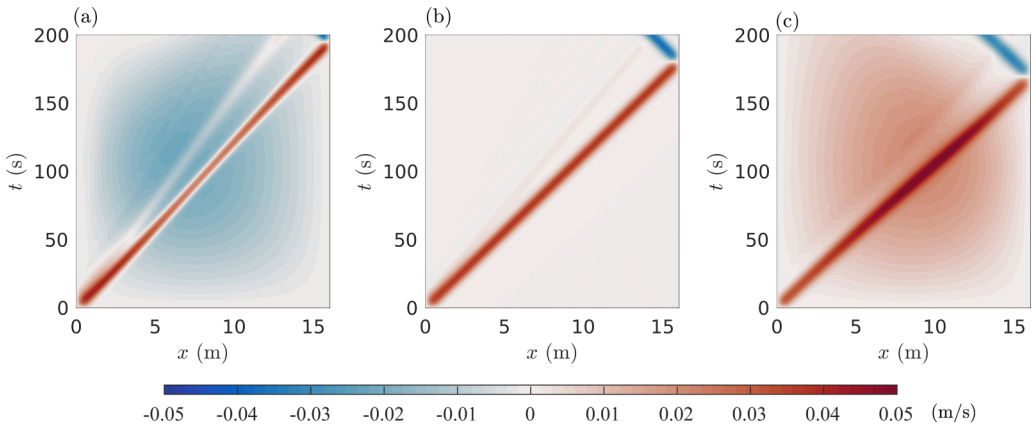

FIG. 3. Hovmöller plots of the horizontal velocity along the inviscid top boundary for the cases (a) C10, (b) I10, and (c) T10.
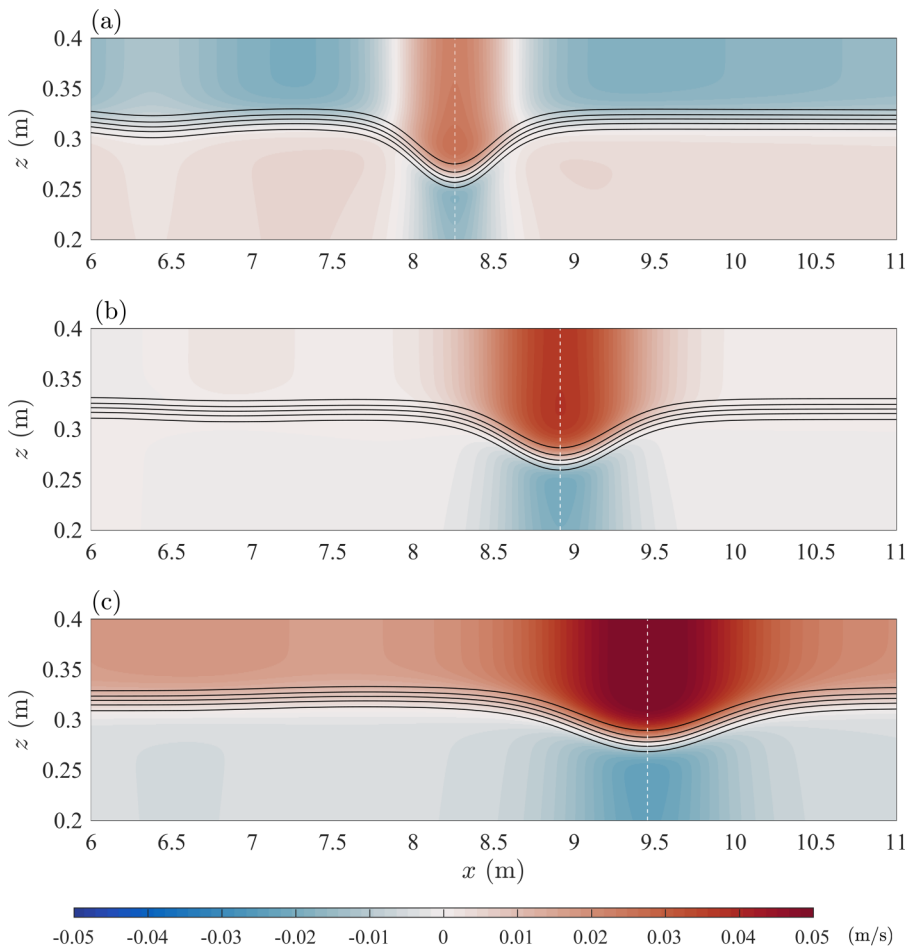
FIG. 4. Horizontal velocity fields of (a) C10, (b) I10, and (c) T10 at $t = 100$ s. The pycnoclines are indicated by the black contours and the waves' crests (determined by the locations of the maximum wave-induced horizontal velocity) are indicated by the dashed lines.

B. Simulation results

We let u_T denote the wave-induced horizontal velocity along the inviscid top boundary. Here the wave-induced velocity is defined as the difference between the total velocity and the background velocity **U**. For internal waves propagating in a domain with free-slip top boundary conditions, the evolution of u_T provides an overview of both the propagation and shape of the waves. For the cases C10, I10, and T10, Hovmöller plots of the total horizontal velocity along the top boundary are given in Fig. 3, where the wave-induced velocity is characterized by the diagonal patterns and can be clearly distinguished from the seiche-induced velocity in the background. In this figure, modulation of the ISWs due to the seiche-induced background currents can be clearly seen. This includes a change in the maximum current induced by the ISWs and the half-width of the ISWs. In particular, there is a decrease in the maximum current and the half-width for the case C10 shown in Fig. 3(a), but an increase in the maximum current and the half-width for the case T10 shown in Fig. 3(c). Also noticeable from this figure is that, as the waves propagate, their shapes are constantly changing in order to adjust to the nonuniform background environment.

Figure 4 shows the waves in the cases C10, I10, and T10 at $t = 100$ s. In this figure, the location of the waves' crest, denoted by x_C, is determined by the locations where the maximum value of u_T

TABLE II. Wave parameters of the ISWs measured at $t = 100$ s, for simulations listed in Table I. Here A_w is amplitude, L_w is half-width, c is propagation speed, and Fr is Froude number.

Case	Dimensional parameters			Dimensionless parameters			
	A_w (10^{-2} m)	L_w (m)	c (10^{-2} m/s)	A_w/H	L_w/H	c/c_{lw}	Fr
Cases in which the ISW is generated at the seiche's crest							
C10	6.25	0.72	8.25	0.156	1.79	1.03	0.253
C15	8.67	0.80	8.73	0.217	2.00	1.09	0.239
C20	10.78	0.92	8.99	0.270	2.30	1.12	0.232
C25	12.34	1.07	9.09	0.309	2.68	1.14	0.230
Cases with ISW only (i.e., no seiche)							
I10	5.32	0.92	8.91	0.133	2.29	1.11	0.234
I15	7.59	1.01	9.26	0.190	2.52	1.16	0.225
I20	9.38	1.16	9.42	0.235	2.91	1.18	0.222
I25	10.71	1.36	9.45	0.268	3.40	1.18	0.221
Cases in which the ISW is generated at the seiche's trough							
T10	4.45	1.16	9.46	0.111	2.90	1.18	0.221
T15	6.33	1.29	9.69	0.158	3.21	1.21	0.215
T20	7.89	1.48	9.76	0.197	3.71	1.22	0.214
T25	8.83	1.74	9.72	0.221	4.34	1.21	0.215

is found, i.e.,

$$u_T(x_C) = \max(u_T). \qquad (10)$$

For the case C10 shown in Fig. 4(a), the wave appears narrower and propagates slower, whereas for the case T10 shown in Fig. 4(c), the wave appears wider and propagates faster. In all cases, the waves are symmetric about their crests and, except for C10, do not have clearly visible trailing waves.

Table II gives the quantitative measurement of the solitary-wave parameters at $t = 100$ s. Here the amplitude A_w is measured based on the height where the maximum buoyancy frequency occurs along the waves' crests, by computing the difference between the simulation results and the background states. The half-width L_w is measured based on u_T by computing the distance between the points x_L and x_R which satisfy the equation

$$u_T(x_L) = u_T(x_R) = 0.5\max(u_T). \qquad (11)$$

The average propagation speed c is estimated based on the location of the waves' crests at $t = 100$ s, according to the formula

$$c = \frac{x_C}{t}. \qquad (12)$$

This estimate is applicable for the instantaneous speed as well since, as shown in Fig. 3, the propagation speed is nearly constant in various background states. The Froude number is defined in the context of internal wave dynamics as

$$\text{Fr} = \frac{U}{c}. \qquad (13)$$

Here we do not use the vertically integrated value of U as it is essentially zero, because the flow is nondivergent in the simulation domain. Instead, we set $U = 0.021$ m/s, which is the maximum background horizontal current at $t = 100$ s. The table shows that for all cases Fr $\ll 1$ and that the flow is subcritical.
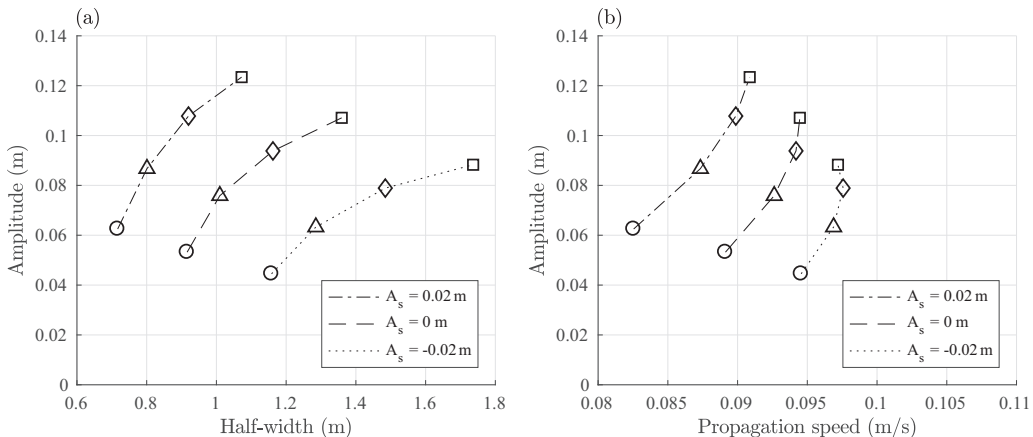
FIG. 5. Visualization of Table II, with amplitude versus (a) half-width and (b) propagation speed for the ISWs at $t = 100$ s. From left to right, circles represent the cases C10, I10, and T10, triangles represent the cases C15, I15, and T15, diamonds represent the cases C20, I20, and T20, and squares represent the cases C25, I25, and T25.

Figure 5 provides a visualization for the wave parameters listed in Table II. In this figure, cases with the same letter in their labels (i.e., those with the same background shear) are connected together by the same curves, while cases with the same number in their labels (i.e., those with the same depression in the initial density fields) are indicated by the same symbols. The figure suggests that, in a given background environment, the wave amplitude increases as the half-width and the propagation speed increase. It also suggests that waves in the cases connected together by a dash-dotted curve have a larger amplitude but a smaller half-width and propagation speed, while waves in the cases connected together by a dotted curve have a smaller amplitude but a larger half-width and propagation speed. Note that the background current in the former cases has a negative vorticity, while that in the latter cases has a positive vorticity. Because the ISW-induced vorticity is positive, results presented in this figure are consistent with those concluded in [6].

We note that the analyses presented above are based on the assumptions that the waves are evolving adiabatically and that the waves have fully adjusted to the local background environment. This assumption is valid because the seiches that form the background state are evolving on space scales and timescales much larger and longer than scales associated with the waves. While a longer tank would enhance such scale separation, Fig. 6 suggests that the ISW in a 32-m tank appears almost exactly the same as that in a 16-m tank. In this figure, the simulation labeled as C10L (not listed in Table I) is set up with exactly the same parameters as those in C10, except that the length of the tank is extended to 32 m. As a result, the wave reaches the center of the tank by $t = 200$ s instead of 100 s in C10. The snapshot of the horizontal velocity field showing the wave at $t = 200$ is thus produced to compare with that at $t = 100$ s in C10. The difference between the two cases, computed by carefully aligning the locations of the waves' crests, is shown in Fig. 6(c). It suggests that there is no significant difference in the horizontal velocity induced by the leading waves, while the difference in the background is due to the different locations of the trailing waves. In fact, the maximum difference along the waves' crests is 2.2×10^{-3} m/s, which is more than an order of magnitude smaller than the wave-induced horizontal velocity. Therefore, the wave dynamics in a 16-m tank is not fundamentally different from that in a 32-m tank, and hence a 16-m tank is long enough for the scale separation between the waves and the seiches.

C. Comparison to exact solitary-wave solutions

Although the terminology ISW is used here, the waves examined in this section are not exact solitary waves, since they are propagating in a spatially and temporally varying background
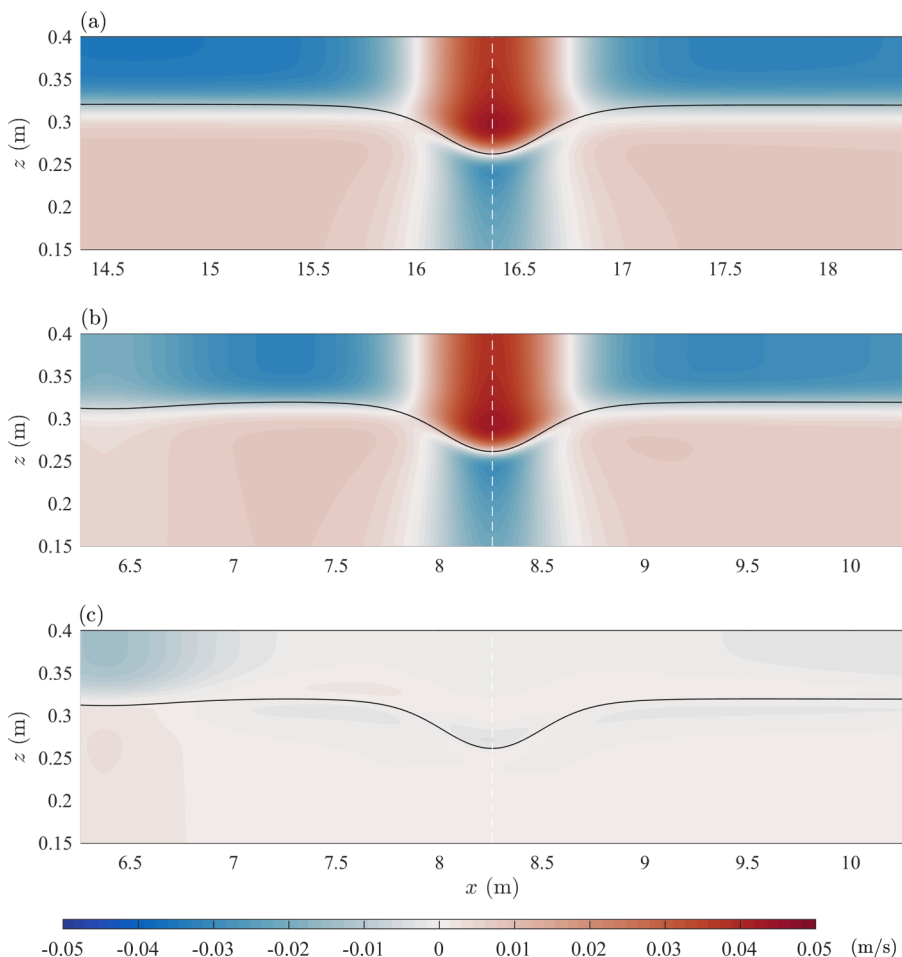
FIG. 6. Comparison of the horizontal velocity fields between (a) C10L at $t = 200$ s and (b) C10 at $t = 100$ s. The difference between (a) and (b), taken by matching the locations of the waves' crests in (a) and (b), is shown in (c). The pycnoclines are indicated by the black curves and the waves' crests are indicated by the dashed lines.

environment. Hence, their waveforms are constantly changing, in order to adjust to the slowly varying background state. To compare the waveform of the ISW in the simulation C10 at $t = 100$ s and that described by the DJL theory, we extracted the density and horizontal velocity profiles from the simulation C0 at $t = 100$ s and $x = 8.259$ m, which corresponds to the location of the ISW's crest in C10 at $t = 100$ s. We then used these profiles as the background state to compute the DJL equation iteratively, using 16 different values of the *scaled* APE between 1.7×10^{-5} and 2×10^{-5} m^2. Figure 7 shows the difference (in absolute values) between the simulation result and the DJL solutions along the wave's crest, as functions of the APE. It suggests that the difference is minimum when the scaled APE is approximately 1.88×10^{-5} m^2, where the normalized difference in ρ and u is approximately 2% and 4.5%, respectively. This implies that the simulation result fits the DJL solutions extremely well, at least at the location along the wave's crest. The difference could be due to the nonsteady, nonuniform nature of the background environment in the simulation, the viscous adjustment of the wave, or simply numerical noise in the DJL solutions.
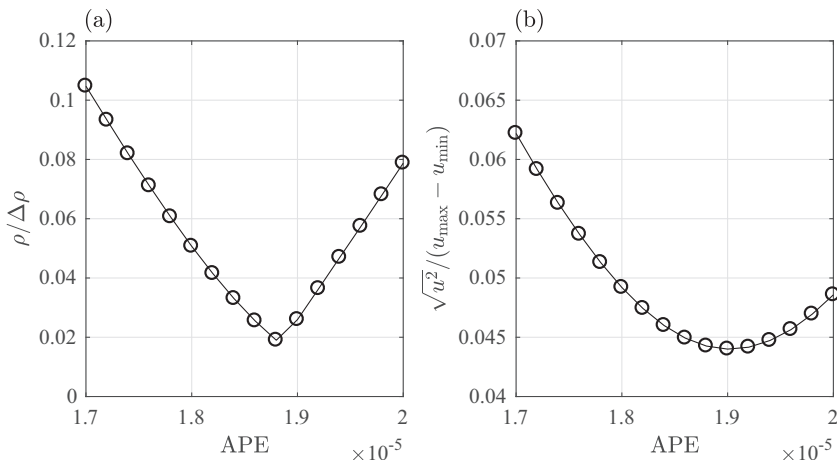
FIG. 7. Comparison of the simulation result to the DJL solutions along the wave's crest, for the case C10 at $t = 100$ s. (a) Maximum difference in ρ normalized by $\Delta\rho$. (b) Root mean square of the difference in u normalized by $[\max(u) - \min(u)]$. Note that the APE is scaled by $\rho_0 gH$ in a two-dimensional domain and is in units of m^2; see Eq. (3).

As the ISW propagates, it is constantly adjusting its form to the background environment upstream of its crest. For this reason, we performed the same analysis by solving for the DJL equation in the background state extracted from C0 at $t = 100$ s and $x = 9.259$ m (i.e., the location 1 m upstream of the wave's crest in C10 at $t = 100$ s). The comparison, although not shown here, suggests that the simulation result fits the DJL solutions slightly better, where the difference is within 2% for the density and 3.5% for the horizontal velocity. The similarity in the DJL solutions is due to the similarity in the background states. Because the seiche has a much larger length scale than the ISW, variation in the seiche-induced background environment is very small near the ISW's crest. However, we note that variation in the seiche-induced background environment depends on the amplitude and wavelength of the seiche, as well as the layer thickness and the pycnocline thickness.

In Fig. 8 we further examine the difference between the simulation result of C10 at $t = 100$ s and the DJL solution computed with the scaled APE of 1.88×10^{-5} m^2 in the background state extracted from C0 at $t = 100$ s and $x = 8.259$ m, by comparing the horizontal velocity fields and the density fields. The figure shows that the difference is small over the majority of the wave body, suggesting that the wave we observed in the simulation can at least be considered as a solitary-like wave, since the majority of the wave body satisfies the DJL solution. In fact, Fig. 8(c) shows that the major difference in the horizontal velocity and density fields comes from the trailing wave near $x = 6.5$ m in the simulation, where the density difference is approximately 0.003 and the velocity difference is approximately 0.008 m/s. Equivalently, these values are approximately 30% of $\Delta\rho$ and 35% of $\max(u)$, respectively.

We have also performed the same analysis for the case C10 at $t = 170$ s. The result is quantitatively similar and hence is not shown here. In particular, the DJL solution that matches the simulation result the best is obtained by specifying the scaled APE to be 1.88×10^{-5} m^2. The fact that it has not changed since $t = 100$ s implies that, as the ISW propagates, there is very little energy transfer between the ISW and the background environment. Additionally, the same analysis has been performed for several other cases. The results are not shown here because all of them suggest a very good match between the simulation results and the DJL solutions. The implication of these results is that, in laboratory experiments, ISWs propagating in a shear background current can be generated by using the lock-release mechanism in a tilted tank.
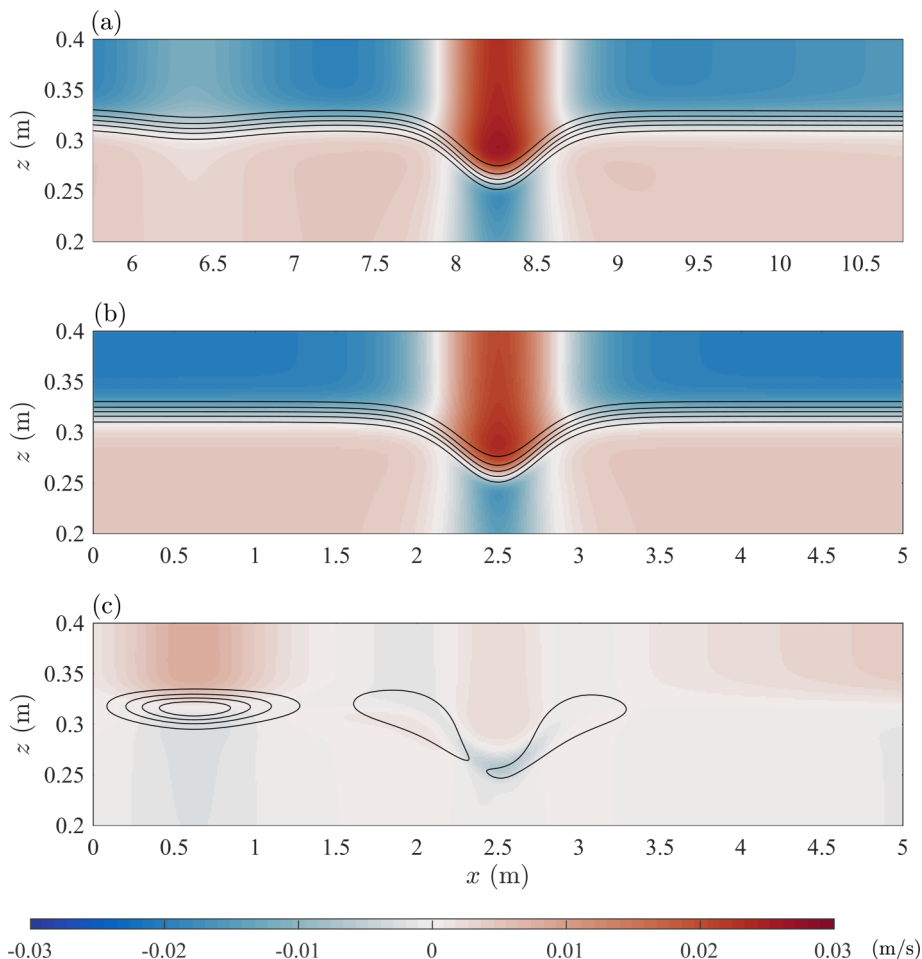
FIG. 8. Horizontal velocity fields in (a) the simulation C10 at $t = 100$ s and (b) the DJL solution, with pycnoclines indicated by the black contours. (c) Difference in the horizontal velocity (pseudocolor) and density (black contours) between the simulation result and the DJL solution, computed by interpolating the velocity and density fields of (a) onto the grid of (b) and then taking the difference.

V. TRANSITION TO DISPERSIVE-WAVE REGIME

A. Gardner equation predictions

As the pycnocline approaches the middepth, there are two possible issues with identifying solitary waves in a finite-length experimental tank. First, it may be the case that no solitary waves form for a given initial condition. Within the framework of the KdV or Gardner equations, this may be done approximately by numerically solving the initial-value problem for a given initial profile or theoretically by solving the scattering problem and determining if there is a discrete spectrum [30,31]. Second, it may be that while solitary waves can form in the asymptotic limit of $t \to \infty$, they will not separate from linear waves and smaller solitary waves before the end of the tank is reached. This point has been addressed in the literature by defining a sorting timescale [31], and we visit this technique below.

In the absence of a background current, one practical way to quantify the first issue is to compute the Gardner equation-predicted solitary-wave width for a range of amplitudes and interface heights,
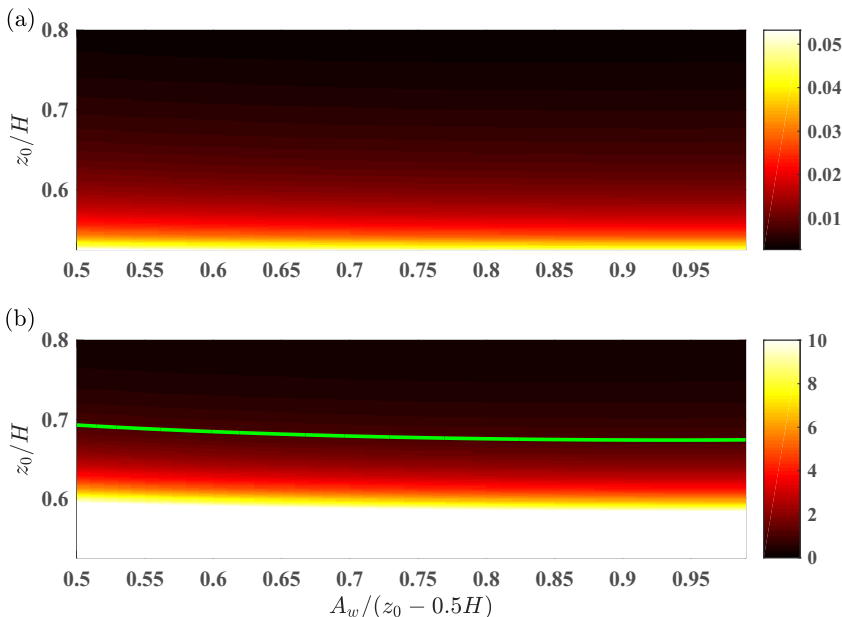
FIG. 9. Shaded contours showing (a) solitary-wave width and (b) separation length between a solitary wave and linear waves, predicted by the Gardner equation for a two-layer fluid. In (b), the curve along which the split length equals the tank length is shown in green. In both panels, the shaded quantities are scaled by the tank's length and shown as functions of dimensionless interface height z_0/H and dimensionless solitary-wave amplitude $A_w/(z_0 - 0.5H)$.

scaled by the tank's length. This is shown in Fig. 9(a). The interface height z_0 is scaled by the total depth H and the solitary-wave amplitude A_w is scaled by the distance from the interface height to the middepth $|z_0 - 0.5H|$ (the so-called conjugate flow amplitude [32]). The numerical tank is chosen to be 100 m long, a value far too large for an experimental configuration, but useful to make the point that the first of the above-mentioned restrictions is of secondary importance in an experimental setting. The figure indicates that the Gardner equation predicts that solitary waves are possible in all cases, and indeed, even with a 20-m-long tank, representative of some cases below, solitary waves would comfortably fit into the domain.

To quantify the second issue we define the sorting length in the following manner: (i) We choose a fraction $0 < f < 1$ of the predicted solitary-wave width γ we want as a target separation between the solitary wave and other waves, (ii) we use the Gardner equation's exact solitary-wave solution to compute the weakly nonlinear estimate of the solitary waves' propagation speed, and (iii) we subtract the linear long-wave speed from the solitary-wave speed and form a separation length scale L_s as

$$L_s = \frac{cf\gamma}{c - c_0}. \qquad (14)$$

This length scale underestimates the length traveled by the waves if two solitary waves of similar size are present (i.e., c_0 would need to be replaced by the propagation speed of the smaller solitary wave for a better estimate) but provides a good qualitative guide. The estimate, scaled by the tank length, is shown in Fig. 9(b). It is clear from this figure that, for the vast majority of cases with a pycnocline near the middepth, even a 100-m-long tank is not long enough for a solitary wave to separate from a tail of linear waves and as such from smaller solitary waves. We note that this scaling is different from the sorting timescale defined by Eq. (18) in [31]. For the surface-wave
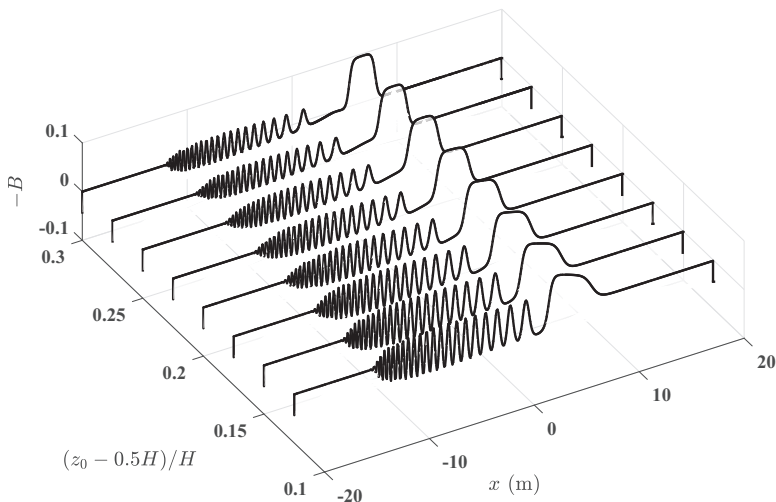
FIG. 10. Predicted waveform from numerical solutions of the Gardner equation after a fixed amount of time as a function of the length along the tank x and the scaled distance between the interface height and the middepth $(z_0 - 0.5H)/H$. For clarity of presentation, we have reversed the amplitude of the solutions so that the waves appear as waves of elevation.

experiments of [31], a scaling based on tank depth and a user-chosen effective length is sensible. In our theory the user-chosen parameter is f, the fraction of the solitary-wave width we want to set as the separation between waves. Our method is based on the exact solution of the Gardner equation, and thus has a more specific purpose than that in [31]; nevertheless, both techniques are similar in spirit.

An interesting question thus follows: What does the Gardner equation predict will happen when the tank is too short for complete sorting? In Fig. 10 we show eight sample numerical solutions of the Gardner equation after the waveform has propagated approximately 20 m. It is clear that as z_0 tends to the middepth, separation from the tail of linear waves is no longer evident, and indeed the leading disturbance loses the hump shape associated with a Gardner solitary wave. These results thus provide the setting for our numerical explorations with the full set of stratified Navier-Stokes equations. While the results based on the Gardner equation are obtained without the presence of a background current, the two suggestions are that (i) the solitary wave should be possible when the pycnocline center lies away from the middepth even when weak shear currents associated with a background seiche are present and (ii) the solitary wave may be lost, on the scale of the experimental tank, when the pycnocline center moves toward the middepth. Moreover, the latter result may be sensitive to the presence of weak shear currents.

B. Parameter space

For simulations presented in this section, parameters of their initial density profiles are given in Table III. Here we explore the parameter space relevant to the background stratification and current by varying z_0 between 0.28 and 0.32 m (i.e., between 0.65 and 0.8 of the total depth) and A_s between -0.04 and 0.02 m. By adjusting z_0, we are essentially adjusting the thickness of the upper and lower layers and hence the influence of dispersion on the waveforms. The two-layer long-wave speed are $c_{lw} = 0.079$, 0.086, 0.091, and 0.094 m/s for $z_0 = 0.32$, 0.3, 0.28, and 0.26 m, respectively. The corresponding Reynolds numbers are not computed individually because they are all on the same order of magnitude as that given in the preceding section. On the other hand, by adjusting A_s, we are essentially adjusting the strength and polarity of the seiche-induced velocity shear in the

TABLE III. List of simulations presented in Sec. V. The dimensionless parameters, labeled with a tilde, are scaled by H. In the case labels, the number following Z indicates the height of the pycnocline (i.e., z_0 in 10^{-2} m), while the dash and number following A indicates the polarity and amplitude of the initial seiche (i.e., A_s in 10^{-2} m).

Case	Dimensional parameters				Dimensionless parameters			
	z_0 (m)	A_s (m)	A_0 (m)	λ_0 (m)	$\tilde{z}_0$	$\tilde{A}_s$	$\tilde{A}_0$	$\tilde{\lambda}_0$
Cases in which the seiche's node is located at $z_0 = 0.32$ m								
Z32A-4	0.32	−0.04	0.14	0.8	0.8	−0.1	0.35	2
Z32A-2	0.32	−0.02	0.14	0.8	0.8	−0.05	0.35	2
Z32A0	0.32	0	0.14	0.8	0.8	0	0.35	2
Z32A2	0.32	0.02	0.14	0.8	0.8	0.05	0.35	2
Cases in which the seiche's node is located at $z_0 = 0.3$ m								
Z30A-4	0.3	−0.04	0.14	0.8	0.75	−0.1	0.35	2
Z30A-2	0.3	−0.02	0.14	0.8	0.75	−0.05	0.35	2
Z30A0	0.3	0	0.14	0.8	0.75	0	0.35	2
Z30A2	0.3	0.02	0.14	0.8	0.75	0.05	0.35	2
Cases in which the seiche's node is located at $z_0 = 0.28$ m								
Z28A-4	0.28	−0.04	0.14	0.8	0.7	−0.1	0.35	2
Z28A-2	0.28	−0.02	0.14	0.8	0.7	−0.05	0.35	2
Z28A0	0.28	0	0.14	0.8	0.7	0	0.35	2
Z28A2	0.28	0.02	0.14	0.8	0.7	0.05	0.35	2
Cases in which the seiche's node is located at $z_0 = 0.26$ m								
Z26A-4	0.26	−0.04	0.14	0.8	0.65	−0.1	0.35	2
Z26A-2	0.26	−0.02	0.14	0.8	0.65	−0.05	0.35	2
Z26A0	0.26	0	0.14	0.8	0.65	0	0.35	2
Z26A2	0.26	0.02	0.14	0.8	0.65	0.05	0.35	2

background. The parameters A_0 and λ_0 are fixed at 0.14 and 0.8 m, respectively. Note that for solitary waves, the wave amplitude and half-width are related and cannot be set separately. By fine-tuning the parameters A_0 and λ_0, we found that the combination $A_0 = 0.14$ m and $\lambda_0 = 0.8$ m allows the initial condition to yield a single-crest solitary wave without visible trailing waves in the simulation Z28A0.

For each of the cases listed in Table III, a corresponding simulation with seiche only (by setting $A_0 = 0$) is also performed (not listed here) in order to provide the background state for quantitative measurement. Although the gradient Richardson number and the Froude number vary for different cases, they are not shown here because the flow regime remains the same as that in Sec. IV for all cases presented in this section.

C. Simulation results

In Fig. 11, the Hovmöller plots of the horizontal velocity along the inviscid top boundary provide an overview of the shape and propagation of the waves in the cases Z32A-4, Z32A0, Z28A-4, and Z28A0. The figure shows that, in the presence of a shear background current (as is the case in Z32A-4 and Z28A-4), there are significant changes in both the shape and propagation of the waves. As these waves propagate, there is an increase in the waves' half-width and wave-induced horizontal velocity, and a production of trailing waves. This implies that these waves are attempting to adjust themselves to the varying background environment and may or may not be able to maintain their solitary-like forms. In particular, the trailing waves form only at a later stage, when the background horizontal velocity becomes large enough. This is a clear indication that the modulation of wave dynamics occurs due to the presence of a shear background current. On the other hand, when there
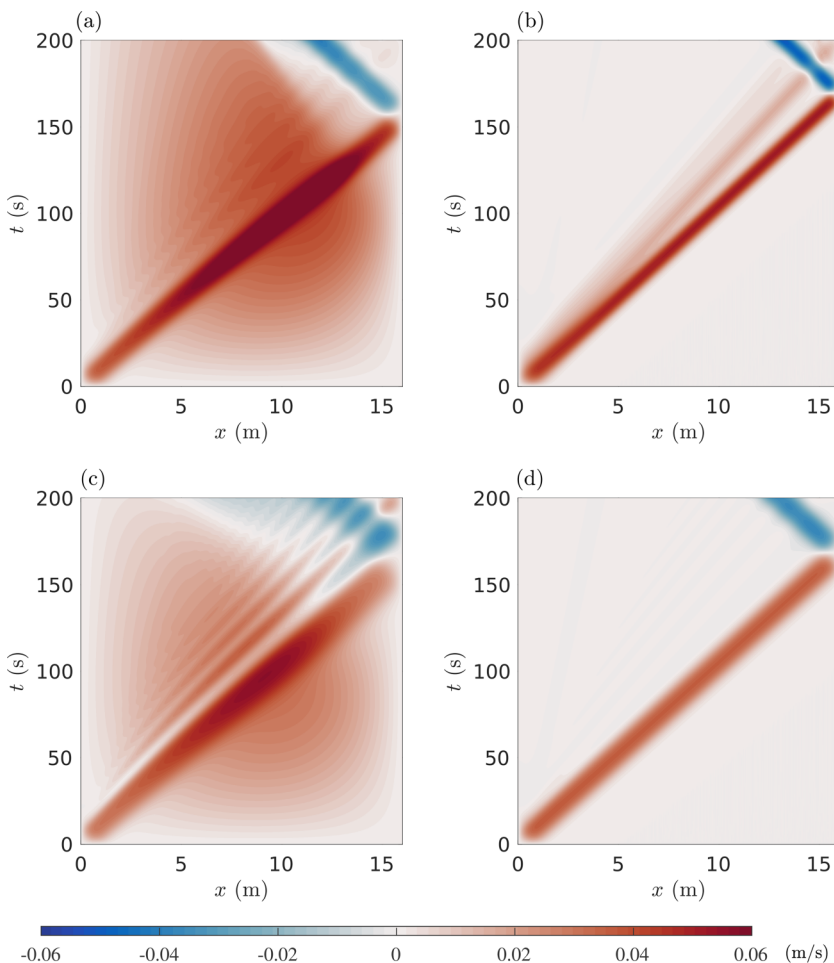
FIG. 11. Hovmöller plots of the horizontal velocity along the inviscid top boundary for the cases (a) Z32A-4, (b) Z32A0, (c) Z28A-4, and (d) Z28A0.

is no background shear (as is the case in Z32A0 and Z28A0), the waves' shape (e.g., half-width and wave-induced horizontal velocity) remains unchanged and their propagation speed remains constant, implying that these waves remain solitary-like as they propagate. While trailing waves can be seen in Z32A0, they are generated together with the leading wave due to the initial depression instead of the presence of a background shear current.

Figure 12 shows the waves in the cases Z32A-4, Z30A-4, Z28A-4, and Z26A-4 at $t = 100$ s. These waves are propagating in shear background currents whose vorticity has the same sign as the wave-induced currents. In the case Z32A-4, the wave is symmetric about its crest and has no trailing waves visible, implying that it is able to maintain its solitary-like form. As the pycnocline approaches the middepth, the leading waves become wider and propagate slower. The increase in the waves' half-width occurs in an asymmetric manner such that the waves flatten toward their front while producing trailing waves of finite amplitude behind them. Judging based on both the pycnocline displacement and the *wave-induced* horizontal velocity, these trailing waves are waves of elevation instead of depression, especially those in the cases Z28A-4 and Z26A-4. The production of trailing waves and the reversal of their polarity appears very similar to that occurred during the fissioning process, in which an ISW of depression shoals upon a gentle slope and produces a DWT
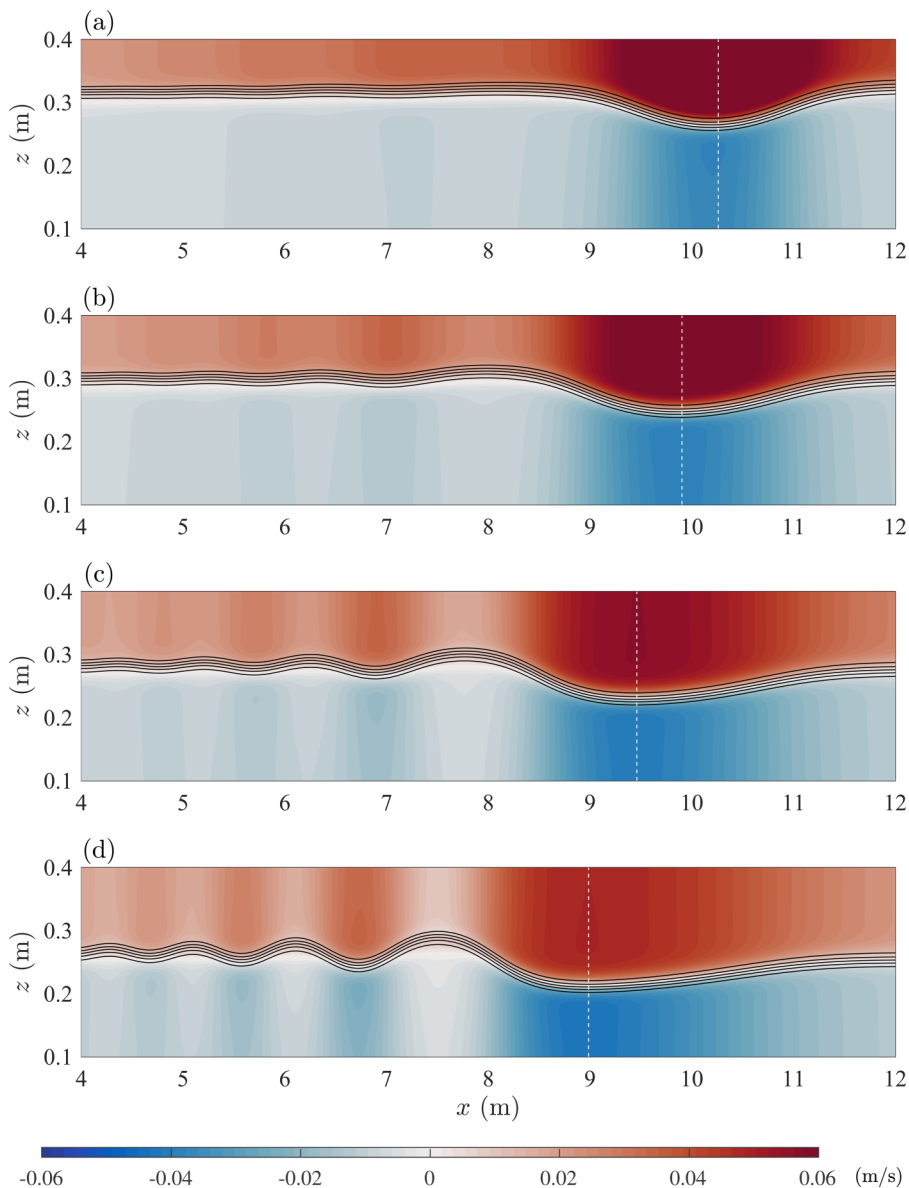
FIG. 12. Horizontal velocity of (a) Z32A-4, (b) Z30A-4, (c) Z28A-4, and (d) Z26A-4 at $t = 100$ s. The pycnoclines are indicated by the black contours and the waves' crests (determined by the locations of the maximum wave-induced horizontal velocity) are indicated by the dashed lines.

(see, for example, Fig. 16 of [33]). Hence, our results suggest that these background states are not able to support the existence of ISWs of depression but can enable the formation of DWTs, even though the pycnocline is above the middepth.

For comparison, Fig. 13 shows the waves in the cases Z32A0, Z30A0, Z28A0, and Z26A0 at $t = 100$ s, in which no background current is present (see also Table IV). The figure suggests that, except for the case Z26A0, waves in all other three cases are solitary-like and have similar propagation speeds. While a trailing wave is observed in the case Z32A0, unlike those shown in Fig. 12, it is a wave of depression instead of elevation and is also solitary-like. In the case Z26A0,
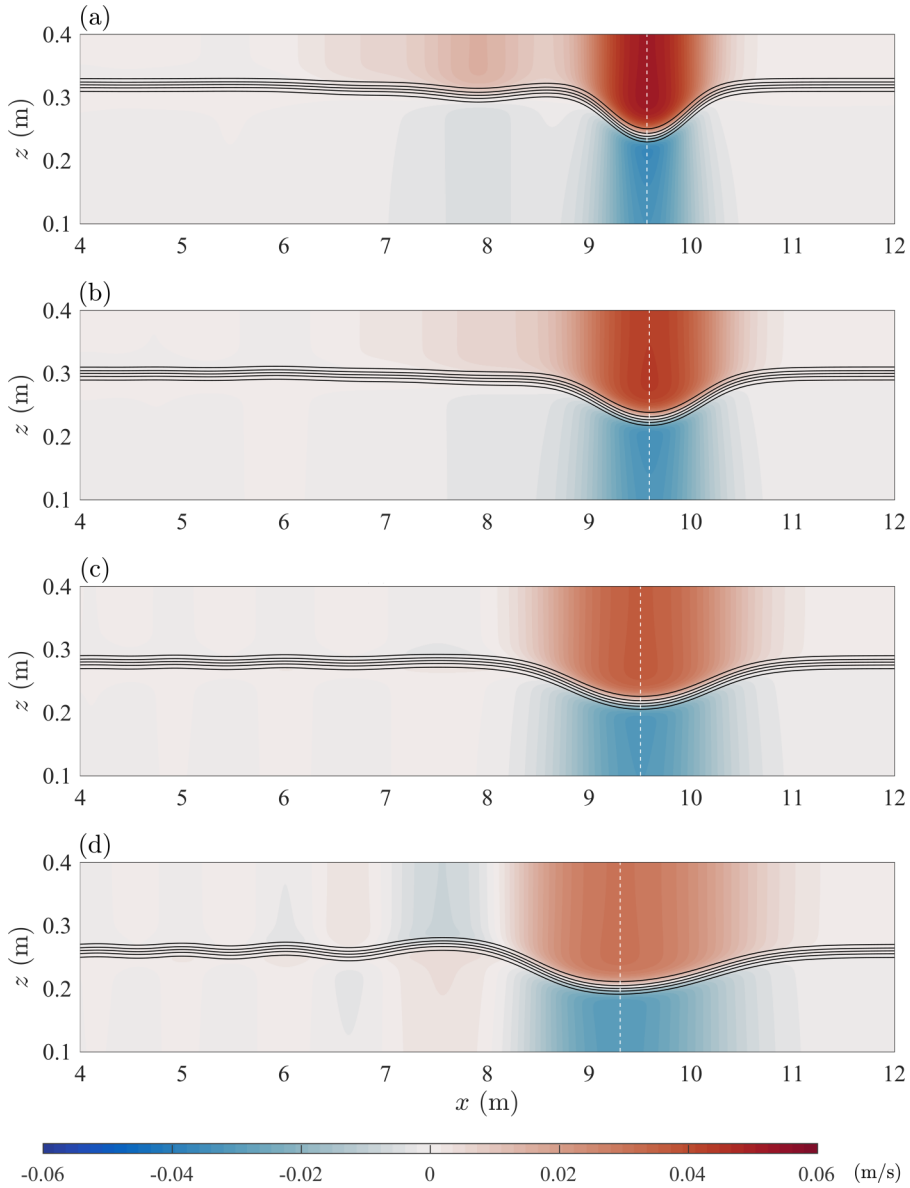
FIG. 13. Same as Fig. 12 but for (a) Z32A0, (b) Z30A0, (c) Z28A0, and (d) Z26A0 at $t = 100$ s.

however, the leading wave is slightly asymmetric about its crest and propagates slower, and the trailing wave has a reversed polarity, implying that a DWT is emerging. The waves in this case are very similar to those in Z30A-4 shown in Fig. 12(b), except for the propagation speed and the wave-induced horizontal velocity. Nevertheless, compared with Z26A-4 shown in Fig. 12(d), in which the pycnocline is centered at a similar depth, the leading wave in Z26A0 appears far less asymmetric and the trailing wave has a much smaller amplitude. Thus, the comparison between Figs. 13 and 12 suggests that, for a given stratification, the presence of a shear background current that has the same vorticity as the wave-induced vorticity increases the dispersive effect such that internal waves propagating in such a background current is less likely to achieve a balance between the nonlinear steepening and dispersive spreading on the scale of the experimental tank.

TABLE IV. Values of c_{lw}, calculated in the absence of a background current, and ω_{wave}, the maximum vorticity induced by the leading wave in the absence of a background current, for the four different pycnocline heights.

Case	Pycnocline height z_0 (m)	Long-wave speed c_{lw} (10^{-2} m/s)	Maximum wave-induced vorticity ω_{wave} (s^{-1})
Z32A0	0.32	7.92	3.15
Z30A0	0.30	8.58	2.76
Z28A0	0.28	9.08	2.42
Z26A0	0.26	9.45	2.17

D. Characteristics of the leading waves

For the simulations presented in this section, Table V gives the quantitative measurement of the parameters of the leading waves at $t = 100$ s. Here the amplitude A_w, half-width L_w, and propagation speed c are defined in the same way as those in Table II. The parameter ω_{max} represents the maximum seiche-induced vorticity (or the minimum vorticity, in cases where it is negative) and is computed from cases without an initial depression. It measures the background shear experienced by the waves, while the ratio $\omega_{\text{max}}/\omega_{\text{wave}}$ measures the strength of the background shear relative to the wave-induced shear. The ratio $(x_R - x_C)/(x_C - x_L)$ measures the asymmetry of the leading waves, where x_C is the location of the waves' crests and satisfies Eq. (10), while x_L and x_R represent

TABLE V. Wave parameters measured at $t = 100$ s, for simulations listed in Table III. Here ω_{max} is calculated from cases without an initial depression and $(x_R - x_C)/(x_C - x_L)$ measures the asymmetry of the leading waves. Values of c_{lw} and ω_{wave} are given in Table IV.

| Case	Dimensional parameters				Dimensionless parameters				
	A_w (10^{-2} m)	L_w (m)	c (10^{-2} m/s)	ω_{max} (s^{-1})	$\dfrac{A_w}{H}$	$\dfrac{L_w}{H}$	$\dfrac{c}{c_{lw}}$	$\dfrac{\omega_{\text{max}}}{\omega_{\text{wave}}}$	$\dfrac{x_R - x_C}{x_C - x_L}$
Cases in which the seiche's node is located at $z_0 = 0.32$ m									
Z32A-4	6.02	1.89	10.23	1.48	0.150	4.72	1.29	0.470	0.99
Z32A-2	7.19	1.45	9.97	0.72	0.180	3.62	1.26	0.229	0.94
Z32A0	8.36	1.09	9.57	0	0.209	2.73	1.21	0	0.98
Z32A2	9.45	0.85	9.06	−0.72	0.236	2.11	1.14	−0.229	1.00
Cases in which the seiche's node is located at $z_0 = 0.3$ m									
Z30A-4	5.62	2.13	9.90	1.34	0.141	5.32	1.15	0.485	1.21
Z30A-2	6.48	1.75	9.82	0.65	0.162	4.38	1.14	0.235	1.01
Z30A0	7.50	1.38	9.59	0	0.188	3.44	1.12	0	0.95
Z30A2	8.67	1.06	9.25	−0.65	0.217	2.64	1.08	−0.235	0.97
Cases in which the seiche's node is located at $z_0 = 0.28$ m									
Z28A-4	5.39	2.31	9.47	1.23	0.135	5.78	1.04	0.507	1.59
Z28A-2	6.02	2.00	9.55	0.60	0.150	5.01	1.05	0.248	1.25
Z28A0	6.80	1.68	9.51	0	0.170	4.20	1.05	0	1.03
Z28A2	7.73	1.34	9.34	−0.60	0.193	3.35	1.03	−0.248	0.96
Cases in which the seiche's node is located at $z_0 = 0.26$ m									
Z26A-4	5.16	2.45	9.00	1.15	0.129	6.13	0.95	0.529	2.06
Z26A-2	5.62	2.21	9.19	0.56	0.141	5.51	0.97	0.258	1.64
Z26A0	6.09	1.94	9.31	0	0.152	4.85	0.98	0	1.28
Z26A2	6.95	1.65	9.31	−0.56	0.174	4.12	0.99	−0.258	1.04
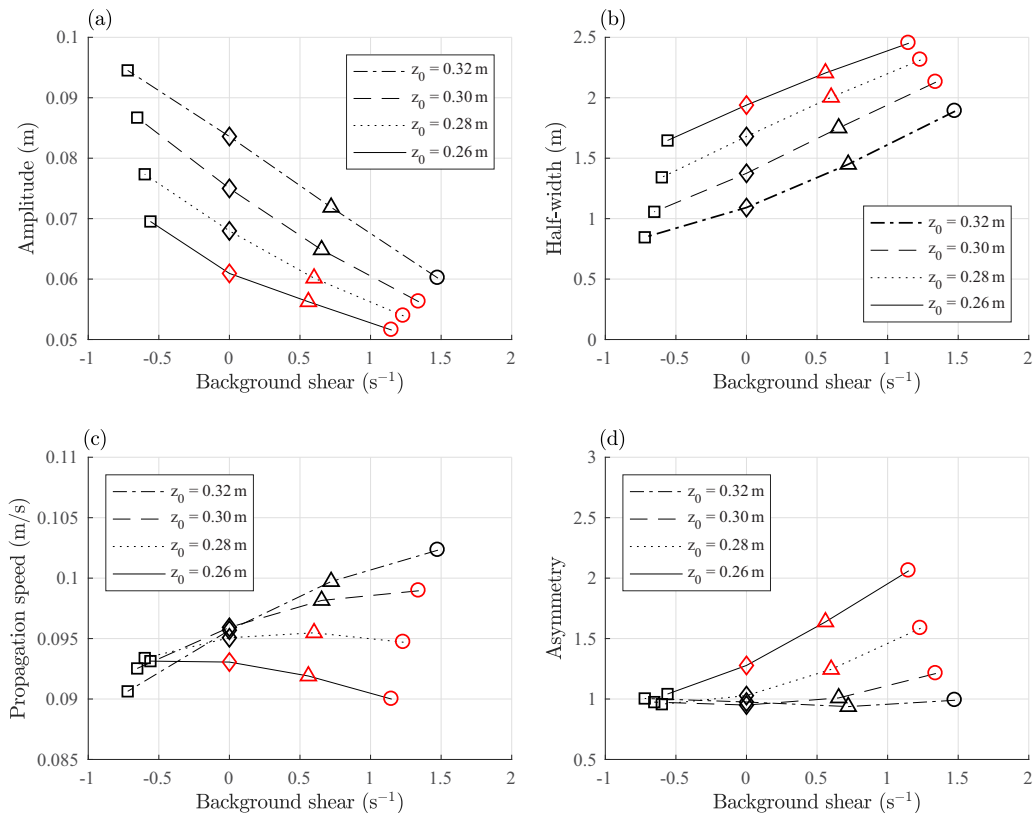
FIG. 14. Visualization of Table V, with (a) amplitude, (b) half-width, (c) propagation speed, and (d) asymmetry of the leading waves versus the background shear at $t = 100$ s. The asymmetry is measured using the ratio $(x_R - x_C)/(x_C - x_L)$, while the background shear is measured based on the seiche-induced vorticity ω_{max}. Cases with similar background shear are indicated by the same symbols, with black (red) symbols indicating the existence of a solitary-like (dispersive) wave.

the downstream (left) and upstream (right) edges of the waves, respectively, and satisfy Eq. (11). If this ratio is close to unity, then the wave is approximately symmetric about its crest and hence is likely to be solitary-like. Otherwise, the wave is asymmetric about its crest due to dispersive effects.

Figure 14 provides a visualization for the parameters listed in Table V. In this figure, cases with similar stratification are connected together by the same curves, while cases with similar background shear are indicated by the same symbols. The figure shows that, for a given stratification, the amplitude and half-width of the leading waves scales approximately linearly with respect to the background shear. In particular, the amplitude decreases as the pycnocline height decreases and as the background shear increases, while the half-width increases as the pycnocline height decreases and as the background shear increases. On the other hand, the propagation speed and the asymmetry of the leading waves do not scale linearly with respect to the stratification or the background shear.

The plot shown in Fig. 14(d) is particularly interesting because the form of the leading waves can be identified from how symmetric they are about their crests. The plot shows that, out of the 16 simulations that we examined, the leading waves in ten of them (indicated by the black symbols) could be solitary-like since the ratio $(x_R - x_C)/(x_C - x_L)$ is close to unity, while those in the remaining six cases (indicated by the red symbols) are dispersive waves since they are asymmetric about their crests. With this information, revisiting Figs. 14(a) and 14(b) suggests that all dispersive waves have an amplitude of $A_w \lesssim 0.06$ m and a half-width of $L_w \gtrsim 2$ m. This implies
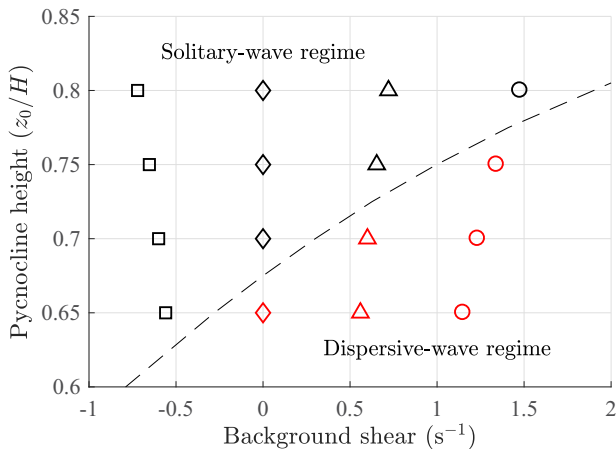
FIG. 15. Stratification (measured by the pycnocline height z_0 scaled by the depth H) versus background shear (measured by ω_{max}) at $t = 100$ s, for simulations listed in Table V. Black (red) symbols indicate cases in which a solitary-like (dispersive) wave exists. The dashed curve indicates the approximate boundary between the solitary-wave regime and the dispersive-wave regime.

that solitary-like waves may only exist if the amplitude is greater than 3% of the half-width, as least in the present model setup. For waves with a more extreme aspect ratio, the dispersive effect becomes dominant. Moreover, revisiting Fig. 14(c) suggests that the solitary-wave propagation speed scales linearly with respect to the background shear, while the propagation speed of the dispersive waves is always smaller. In particular, for cases in which the background vorticity is non-negative, the propagation speed decreases as the pycnocline approaches the middepth. While this seems counterintuitive to the fact that the long-wave speed c_{lw} increases as the pycnocline approaches the middepth, it in fact indicates the transition from the solitary-wave regime to the dispersive-wave regime. For example, for the case Z28A0 which has a pycnocline at $z_0 = 0.26$ m and a zero background vorticity, the two-layer long-wave speed is $c_{lw} = 0.0908$ m/s, smaller than the leading wave's propagation speed of $c = 0.0951$ m/s. In contrast, the two-layer long-wave speed for the case Z26A0 (indicated by the red diamond) is $c_{lw} = 0.0945$ m/s, larger than the leading wave's propagation speed of $c = 0.0931$ m/s. This suggests that the leading wave in Z28A0 is likely a solitary wave but that in Z26A0 is not.

Based on the information obtained from Fig. 14, we are able to determine the solitary-wave regime and the dispersive-wave regime for waves in the 16 cases examined in this section. Figure 15 shows these cases on the plane of stratification-background shear, with cases in which solitary-like waves exist located at the upper left part of the plane and cases in which dispersive waves exist located at the lower right part of the plane. This means that, for large-amplitude nonlinear internal waves propagating in a quasi-two-layer stratification, the balance between the nonlinear steepening and the dispersive spreading (and hence the waveforms of these waves) is determined by the combined effect of the stratification and the background shear. In a stratification in which the pycnocline is relatively far away from the middepth, or a background shear current whose vorticity has the opposite sign to the wave-induced vorticity, such a balance is relatively easily maintained such that solitary and solitary-like waves are more likely to exist. On the other hand, if the pycnocline is close to the middepth or the background vorticity has the same sign as the wave-induced vorticity, then dispersive spreading tends to be the dominant effect, such that DWTs are more likely to form instead. However, we note that the exact boundary between the solitary-wave regime and the dispersive-wave regime could be dependent on the particular model setup and is likely to be sensitive to the length scales and timescales of the experiments.

TABLE VI. Wave parameters of five different ISWs obtained by solving for the DJL equation in the background environment of the case Z26A-4 at $t = 100$ s and $x = 9$ m. Here the APE is scaled by $\rho_0 g H$ in a two-dimensional domain and is determined according to Eq. (3). The two-layer long-wave speed for this stratification in a zero background current is $c_{lw} = 0.0945$ m/s.

Scaled APE	Dimensional parameters			Dimensionless parameters		
(10^{-4} m^2)	η_{max} (10^{-2} m)	L_w (m)	c (10^{-2} m/s)	η_{max}/H	L_w/H	c/c_{lw}
0.2	2.06	5.39	10.18	0.052	13.48	1.078
0.5	2.97	6.20	10.17	0.074	15.51	1.076
1	3.87	6.80	10.13	0.097	16.99	1.072
2	5.14	7.23	10.03	0.128	18.09	1.062
5	7.73	7.58	9.70	0.193	18.95	1.026

E. Exact solitary waves in the dispersive-wave regime

To determine the waveforms of exact solitary waves in the dispersive-wave regime and to compare and contrast them to those of the dispersive waves observed in the simulations, we computed the solutions of the DJL equation using the background profiles of the case Z26A-4 at $t = 100$ s and $x = 9$ m, which corresponds to the location of the leading wave's crest. We considered five different values of the scaled APE from $A = 2 \times 10^{-5}$ to 5×10^{-4} m^2 and recorded parameters of the five different waves in Table VI and Fig. 16. Here the amplitude is measured by η_{max}, the maximum value of (the absolute value of) the isopycnal displacement. It is similar though not exactly equivalent to A_w reported previously, which is measured based on the location of the maximum buoyancy frequency. The table and figure show that, in such a background environment, exact solitary waves have an extremely large half-width, which increases as the amplitude increases, while their propagation speed is relatively constant. The wave computed using $A = 2 \times 10^{-4}$ m^2 has an amplitude of 0.0514 m, similar to that of the dispersive wave in the simulation Z26A-4 at $t = 100$ s. Nevertheless, it has a half-width of 7.23 m and a propagation speed of 0.1003 m/s. In contrast, the wave in Z26A-4 has a half-width of only 2.45 m and a propagation speed of 0.0900 m/s. Although this wave is the widest in all of the 16 cases we examined, it is still much narrower than the exact solitary wave in this background environment. This implies that the main reason that the wave in the simulation remains dispersive is that, for the given length scales and timescales of the
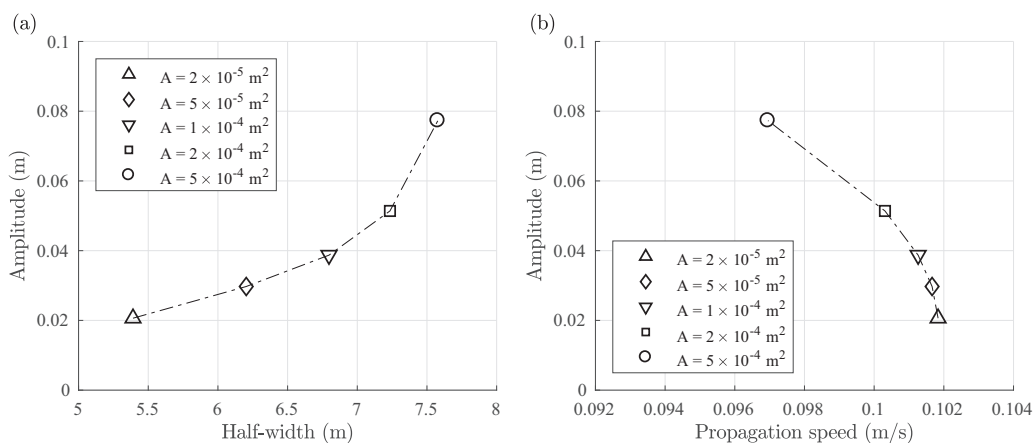

FIG. 16. Amplitude versus (a) half-width and (b) propagation speed for five different ISWs obtained by solving for the DJL equation in the background environment of the case Z26A-4 at $t = 100$ s and $x = 9$ m.

present model setup (note that the length of the domain is $L = 16$ m), it is not able to successfully adjust to the background environment.

VI. CONCLUSION AND DISCUSSION

In the present work, we studied large-amplitude internal waves propagating in shear background currents induced by basin-scale internal seiches, using high-resolution direct numerical simulations performed on the laboratory scale. By varying the parameters of the initial density stratification, we observed the formation of both ISWs and DWTs in the simulations. For simulations in which ISWs are formed, the characteristics of the waves are similar to those examined in [6]. More specifically, the ISWs tend to have a smaller amplitude and a larger half-width if the background vorticity has the same sign as the ISW-induced vorticity and vice versa. Comparison to waveforms of exact solitary waves obtained by solving for the DJL equation suggests that the ISWs in the simulations are indeed solitary-like, implying that ISWs propagating in a shear background current can be generated in a similar manner in laboratory experiments. Further to the above observations, we found that if the leading wave's amplitude is less than approximately 3% of the wave's half-width, then the dispersive effect outweighs the nonlinear effect and a DWT is formed. The transition from the solitary-wave regime to the dispersive-wave regime occurs gradually, as the pycnocline approaches the middepth and as the background vorticity increases from negative to positive, provided the wave-induced vorticity is positive. Solving for the DJL equation in the dispersive-wave regime suggests that exact solitary waves with similar amplitude are much longer and have a more extreme aspect ratio such that their waveforms cannot be supported by the finite length of the computational domain. Both simulations and DJL theory are qualitatively consistent with results for the weakly nonlinear Gardner equation. The Gardner equation allows for the derivation of two theoretical restrictions on the appearance of ISWs for a given set of parameters. The first is whether ISWs are possible for a given set of initial conditions (i.e., the scattering problem), while the second is whether ISWs leave behind smaller waves and the tail of linear waves on the scale of a given tank. We showed that on experimental scales the second is the more robust restriction.

For nonlinear internal waves, the nonlinear effect decreases as the amplitude decreases while the dispersive effect decreases as the wavelength increases [3]. Because the presence of a shear background current (that has the same vorticity as the wave-induced vorticity) restricts the maximum amplitude an ISW can attain [6], the wave must increase its half-width in order for the dispersive effect to be balanced by the weaker nonlinear effect. This is the reason why ISWs in the dispersive-wave regime tend to have an extreme aspect ratio. Nevertheless, the fact that ISWs of an extreme aspect ratio may not exist in a laboratory-scale domain of finite length does not preclude the possibility of their existence in the field. This is because if the length scales and timescales are sufficiently large, then the leading waves in the DTWs may be able to successfully separate themselves from the trailing waves and become solitary-like. However, in the field more exotic situations are possible due to the interactions of waveforms from multiple sources, and hence it remains a question whether a uniform steady shear that supports the formation of ISWs in the dispersive-wave regime will present. Thus, the scaling up of the present work to field scales is a clear challenge for future study.

Although not discussed in Sec. V, we conjecture that for a given background environment, the waveforms also depend on the waves' amplitude. For waves with a smaller amplitude, the wave-induced current is weaker, meaning that the influence of the background current is larger. Hence, these waves tend to be dispersive instead of solitary-like if the background vorticity has the same sign as the wave-induced vorticity. On the plane of pycnocline height versus background vorticity shown in Fig. 15, the curve separating the solitary-wave regime and the dispersive-wave regime would be steeper. On the other hand, the situation is more complicated for waves with a larger amplitude. This is because the maximum amplitude that an ISW can attain and the maximum current that an ISW can induce are both limited by certain asymptotic limits [34], provided there is no significant stratification near the top and bottom boundaries (as is the case in our simulations).

Moreover, such limiting behavior can be altered by the strength of the background shear that an ISW experiences [6]. Exploring the dependence of waveforms on the waves' amplitude in a shear background current is another potential research topic for future work.

We note that in the present work we did not observe the breaking of any ISWs, since breaking occurs when there is significant stratification near the top or bottom boundary [35,36], though the DJL theory predicts that the occurrence of wave breaking can also be significantly influenced by the presence of a shear background current [6]. The breaking of ISWs is typically accompanied by the formation of a trapped core, which may induce significant instability in the water column and the bottom boundary layer and hence contribute to the material mixing and sediment resuspension [9]. Developing a viable method for studying wave breaking in the presence of a shear background current in a laboratory environment is also a clear avenue for future research. This requires further exploration of the parameter space, including the thickness of the pycnocline, and potential modification of the model setup. The goal would be to identify the regime of breaking waves in Fig. 15.

[1] S. Sarkar and A. Scotti, From topographic internal gravity waves to turbulence, Annu. Rev. Fluid Mech. **49**, 195 (2017).

[2] L. A. Ostrovsky and Y. A. Stepanyants, Do internal solitons exist in the ocean? Rev. Geophys. **27**, 293 (1989).

[3] K. R. Helfrich and W. K. Melville, Long nonlinear internal waves, Annu. Rev. Fluid Mech. **38**, 395 (2006).

[4] M. H. Orr and P. C. Mignerey, Nonlinear internal waves in the South China Sea: Observation of the conversion of depression internal waves to elevation internal waves, J. Geophys. Res. **108**, 3064 (2003).

[5] E. L. Shroyer, J. N. Moum, and J. D. Nash, Observations of polarity reversal in shoaling nonlinear internal waves, J. Phys. Oceanogr. **39**, 691 (2009).

[6] M. Stastna and K. G. Lamb, Large fully nonlinear internal solitary waves: The effect of background current, Phys. Fluids **14**, 2987 (2002).

[7] K. G. Lamb and D. Farmer, Instabilities in an internal solitary-like wave on the Oregon shelf, J. Phys. Oceanogr. **41**, 67 (2011).

[8] D. Bogucki, T. Dickey, and L. G. Redekopp, Sediment resuspension and mixing by resonantly generated internal solitary waves, J. Phys. Oceanogr. **27**, 1181 (1997).

[9] L. Boegman and M. Stastna, Sediment resuspension and transport by internal solitary waves, Annu. Rev. Fluid Mech. **51**, 129 (2019).

[10] S. A. Thorpe, An experimental study of critical layers, J. Fluid Mech. **103**, 321 (1981).

[11] D. A. Horn, J. Imberger, and G. N. Ivey, The degeneration of large-scale interfacial gravity waves in lakes, J. Fluid Mech. **434**, 181 (2001).

[12] A. Grace, M. Stastna, and F. J. Poulin, Numerical simulations of the shear instability and subsequent degeneration of basin scale internal standing waves, Phys. Rev. Fluids **4**, 014802 (2019).

[13] J. Grue, A. Jensen, P.-O. Rusas, and J. K. Sveen, Properties of large-amplitude internal waves, J. Fluid Mech. **380**, 257 (1999).

[14] D. Fructus, M. Carr, J. Grue, A. Jensen, and P. A. Davies, Shear-induced breaking of large internal solitary waves, J. Fluid Mech. **620**, 1 (2009).

[15] M. Carr, J. Franklin, S. E. King, P. A. Davies, J. Grue, and D. G. Dritschel, The characteristics of billows generated by internal solitary waves, J. Fluid Mech. **812**, 541 (2017).

[16] J. L. Hammack and H. Segur, Modelling criteria for long water waves, J. Fluid Mech. **84**, 359 (1978).

[17] M. Carr (private communication).

[18] K. G. Lamb, in *The 1998 WHOI/IOS/ONR Internal Solitary Wave Workshop: Contributed Papers*, edited by T. F. Duda and D. M. Farmer (Woods Hole Oceanography Institute, Woods Hole, 1999), pp. 209–217.

[19] K. G. Lamb, Proceedings of the 14th 'Aha Huliko'a Hawaiian Winter Workshop, 2005 (unpublished), pp. 109–117.

[20] K. G. Lamb and L. Yan, The evolution of internal waves undular bores: Comparisons of a fully nonlinear numerical model with weakly nonlinear theory, J. Phys. Oceanogr. **26**, 2712 (1996).

[21] M. Dunphy, C. Subich, and M. Stastna, Spectral methods for internal waves: Indistinguishable density profiles and double-humped solitary waves, Nonlinear Process. Geophys. **18**, 351 (2011).

[22] B. Turkington, A. Eydeland, and S. Wang, A computational method for solitary internal waves in a continuously stratified fluid, Stud. Appl. Math. **85**, 93 (1991).

[23] M. Stastna and W. R. Peltier, On the resonant generation of large-amplitude internal solitary and solitary-like waves, J. Fluid Mech. **543**, 267 (2005).

[24] P. K. Kundu, I. M. Cohen, and D. R. Dowling, *Fluid Mechanics*, 5th ed. (Academic, New York, 2012).

[25] C. J. Subich, K. G. Lamb, and M. Stastna, Simulation of the Navier-Stokes equations in the three dimensions with a spectral collocation method, Int. J. Numer. Mech. Fluids **73**, 103 (2013).

[26] L. N. Trefethen, *Spectral Methods in Matlab* (Society for Industrial and Applied Mathematics, Philadelphia, 2000).

[27] C. Xu, M. Stastna, and D. Deepwell, Spontaneous instability in internal solitary-like waves, Phys. Rev. Fluids **4**, 014805 (2019).

[28] P. J. Diamessis and L. G. Redekopp, Numerical investigation of solitary internal wave-induced global instability in shallow water benthic boundary layers, J. Phys. Oceanogr. **36**, 784 (2005).

[29] R. S. Arthur and O. B. Fringer, The dynamics of breaking internal solitary waves on slopes, J. Fluid Mech. **761**, 360 (2014).

[30] P. G. Drazin and R. S. Johnson, *Solitons: An Introduction*, 2nd ed. (Cambridge University Press, Cambridge, 1989).

[31] J. L. Hammack and H. Segur, The Korteweg–de Vries equation and water waves. Part 2. Comparison with experiments, J. Fluid Mech. **65**, 289 (1974).

[32] K. G. Lamb, Conjugate flows for a three-layer fluid, Phys. Fluids **12**, 2169 (2000).

[33] P. Aghsaee, L. Boegman, and K. G. Lamb, Breaking of shoaling internal solitary waves, J. Fluid Mech. **659**, 289 (2010).

[34] K. G. Lamb and B. Wan, Conjugate flows and flat solitary waves for a continuously stratified fluid, Phys. Fluids **10**, 2061 (1998).

[35] K. G. Lamb, A numerical investigation of solitary internal waves with trapped cores formed via shoaling, J. Fluid Mech. **451**, 109 (2002).

[36] K. G. Lamb, Shoaling solitary internal waves: On a criterion for the formation of waves with trapped cores, J. Fluid Mech. **478**, 81 (2003).

[37] www.computecanada.ca